

This is a postprint version of the following published document:

Rodriguez-Millan, M., Garcia-Gonzalez, D., Rusinek, A., Abed, F. & Arias, A. (2018). Perforation mechanics of 2024 aluminium protective plates subjected to impact by different nose shapes of projectiles. *Thin-Walled Structures*, vol. 123, pp. 1-10.

DOI: [10.1016/j.tws.2017.11.004](https://doi.org/10.1016/j.tws.2017.11.004)

© 2017 Elsevier Ltd.



This work is licensed under a [Creative Commons Attribution-NonCommercial-NoDerivatives 4.0 International License](https://creativecommons.org/licenses/by-nc-nd/4.0/).

1 **Perforation mechanics of 2024 aluminium protective plates subjected to impact by different nose**
2 **shapes of projectiles**

3 M. Rodriguez-Millan^{a*}, D. Garcia-Gonzalez^{b,c}, A. Rusinek^d, F. Abed^e, A. Arias^b

4 ^a *Department of Mechanical Engineering, University Carlos III of Madrid, Avda. de la Universidad 30, 28911*
5 *Leganés, Madrid, Spain*

6 ^b *Department of Continuum Mechanics and Structural Analysis, University Carlos III of Madrid, Avda. de la*
7 *Universidad 30, 28911 Leganés, Madrid, Spain*

8 ^c *Department of Engineering Science, University of Oxford, Parks Road, Oxford OXI 3PJ, UK*

9 ^d *Laboratory of Microstructure Studies and Mechanics of Materials (LEM3), Lorraine University, 1 route d'Ar*
10 *Laquenexy, 57078 Metz Cedex 3, France*

11 ^e *Department of Civil Engineering, American University of Sharjah, P.O. Box 26666 Sharjah, U.A.E.*

12 * *corresponding author*

13 *Email address: mrmillan@ing.uc3m.es(M.Rodríguez-Millán)*

14 *Phone number: +34916245860*

15 **ABSTRACT:**

16 This paper focuses on the mechanical behaviour of aluminium alloy 2024-T351 under impact loading.
17 This study has been carried out combining experimental and numerical techniques. Firstly,
18 experimental impact tests were conducted on plates of 4 mm of thickness covering impact velocities
19 from 50 m/s to 200 m/s and varying the stress state through the projectile nose shape: conical,
20 hemispherical and blunt. The mechanisms behind the perforation process were studied depending on
21 the projectile configuration used by analyzing the associated failure modes and post-mortem
22 deflection. Secondly, a numerical study of the mechanical behaviour of aluminium alloy 2024-T351
23 under impact loading was conducted. To this end, a three-dimensional model was developed in the
24 finite element solver ABAQUS/Explicit. This model combines Lagrangian elements with Smoothed
25 Particle Hydrodynamics (SPH) elements. A good correlation was obtained between numerical and
26 experimental results in terms of residual and ballistic limit velocities.

27 **KEYWORDS:**

28 AA 2024-T351 · Perforation · Ballistic limit · Energy absorption · FEM-SPH

29

30 **Highlights**

- 31 • The ballistic limit for different projectile shapes has been determined.
- 32 • Different failure modes have been observed depending on the stress state associated to
33 projectile shape.
- 34 • Local effects were more important for conical and hemispherical nose projectiles.
- 35 • A 3D numerical model has been used to simulate the impact tests on plates.
- 36 • Good agreement has been found between experiments and FE simulations.

37 **1. Introduction**

38

39 The impact-protective capacity of structural components has become a relevant requirement for the
40 automotive and aerospace industries. Both energy absorption and crashworthiness concepts are
41 essential for the development of new vehicles and aircraft. In such applications, design challenges are
42 focused on structural crashworthiness and light-weight vehicles. Accordingly, research on
43 crashworthiness has managed to considerably reduce fatalities by 26% in the USA from 2005 to 2011
44 [1].

45

46 Several studies have been carried out to study the impact behaviour of metallic plates. In this field, the
47 research developed by Borvik and co-authors [2-4] and Gupta and co-authors [5-6] can be highlighted
48 because of their relevance. Their work focused on mechanical variables that govern the penetration
49 process, such as the target material, target dimensions, projectile nose shape and impact velocity. In
50 this regard, the projectile-nose determines the stress state and its effect varies with several
51 parameters such as the thickness of the target plate, impact velocity, target thickness to projectile
52 diameter ratio and nose angle or nose radius of the projectiles [7-12]. However, there still remains a
53 need for a systematic study of the influence of projectile nose shape on global deformations (plate
54 deflection, bending and membrane stretching) and local deformations (ductile hole formation,
55 petalling, plugging, rear bulging, discing, tensile tearing, thinning, shear banding and necking) of
56 aluminium plates under impact loading. The study of energy absorption capacity on metallic plates can
57 provide relevant information on the effects of local impacts on the global structural response. This
58 work focuses on the perforation process of a ductile plate of AA2024-T3 when it is subjected to an
59 impact of a non-deformable projectile. To the authors' knowledge, none of the previous impact and
60 perforation studies of AA2024-T3 investigated the effect of the projectile shape on the material
61 response, while keeping the same kinetic energy and boundary conditions. The new experimental data
62 of residual velocities for AA2024-T3 presented in this study can be very useful and relevant especially
63 for the design and optimization of protective structures.

64

65 Finite Element Method (FEM) has been commonly used to simulate impact problems. This method
66 provides models that predict residual velocities, ballistic limits and failure mechanisms depending on
67 the projectile-target configurations [13-18]. Most of the previous studies did not focus on quantifying
68 the amount of global and local energy absorption during the impact process. A common problem in
69 FEM is the excessive element distortions encountered in dynamic loading simulations [19]. Element
70 deletion approach could be used to erode highly distorted elements but presents inconsistencies and
71 no physical fundamentals [20]. In order to minimize this problem, several authors [21-22] described
72 the advantage of using adaptive meshing algorithm as an alternative technique for the analysis of
73 plate-impact events. The scheme of the adaptive mesh available in some commercial FE software (e.g.,
74 ABAQUS [23]) combines the features of Lagrangian and Eulerian analyses which allows for obtaining a
75 high mesh quality during the whole simulation. However, the adaptive remeshing technique is
76 computationally expensive and can lead to numerical instabilities and unexpected termination of the
77 simulation [24]. A mesh-free Smoothed Particle Hydrodynamics (SPH) technique presents several
78 advantages over conventional FEM and can be also used for impact problems [25]. This avoids extreme
79 mesh distortions in problems that involve impact and penetration. However, SPH technique
80 encounters several difficulties in engineering problems such as tensile instability; difficulty in loading
81 essential boundary condition and high computational cost. A new computational method has been

82 recently proposed to fill the gap between conventional FEM and models based on SPH. This method is
83 based on a Lagrangian mesh whose elements are converted into SPH elements when a *conversion*
84 *variable* (strain, stress or any state variable) reaches a critical value. By this way, some distortion- and
85 instability-related problems are avoided without introducing a too expensive computational cost. This
86 approach assumes a rigid coupling between SPH particles and Lagrangian nodes at the interface zone
87 [22;25-27]. The rigid interface definition, however, induces some problems, particularly at highly
88 localized regions as discussed in detail by Zhang and co-authors [26]. This novel approach has been
89 used to simulate high velocity impact computations [28], and is employed in this work for the
90 numerical analysis. In addition to the advantages mentioned above, this method allows also for
91 retaining the mass and mechanical properties of the elements converted into SPH particles.

92

93 The main objective of this research is the analysis of failure mechanisms of aluminium alloy 2024-T531
94 plates perforated by rigid projectiles of different nose shapes. Perforation tests were conducted using
95 conical, hemispherical and blunt projectiles covering impact velocities from 50 m/s to 200 m/s. The
96 experimental arrangement enables the determination of the impact velocity, the residual velocity and
97 the failure mode of the aluminium plates. The experimental results were used to validate and identify
98 the value of the mechanical variable that controls the conversion FEM- SPH method. Once the
99 numerical model was validated with experimental data, it was used to analyse energy absorption
100 mechanisms associated with the deformation and failure of the aluminium plates. In addition, both
101 experimental and numerical techniques allowed for investigating the influence of impact velocity,
102 target thickness and projectile nose shape on the failure mechanisms. The outcomes of this work
103 provide new insights into the energy absorption and failure mechanisms behind the perforation
104 process of AA2024 which allow for a better comprehension of its mechanical response under different
105 impact conditions. The results presented herein provide new relevant information for the design of
106 structures potentially subjected to impact loading such as aeronautical components.

107 **2. Experimental Program**

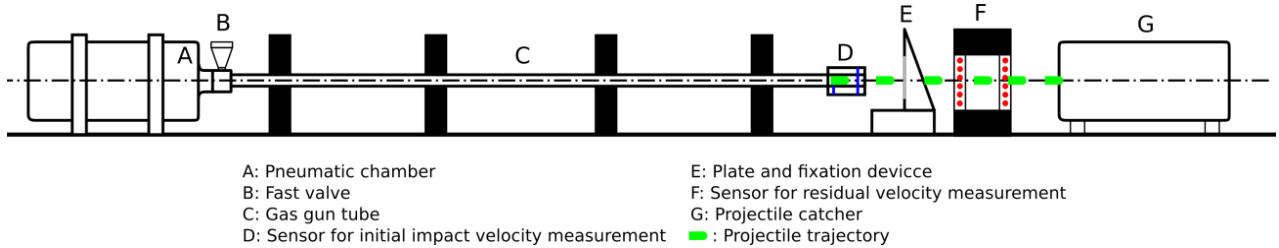
108 **2.1 Material**

109 In the present investigation, the attention is focused on the mechanical behaviour of aluminium alloy
110 (AA) 2024-T351. The principal applications of this material are aircraft structural components, wing
111 tension members, hardware, truck wheels, scientific instruments, veterinary and orthopaedic braces
112 and equipment, and in rivets because of its high strength, excellent fatigue resistance and good
113 strength-to-weight ratio. The AA 2024 T-351 has been widely studied in terms of mechanical behaviour
114 as well as ductile failure (see a previous work of Rodríguez-Millán and co-authors [29]), but its
115 mechanical behaviour against impact loading has not been analyzed enough. Prior to conducting the
116 impact tests, some experiments were conducted under quasi-static conditions in order to verify the
117 material used and its similarities with the one employed in previous published studies (see Appendix
118 A).

119 **2.2 Test set-up**

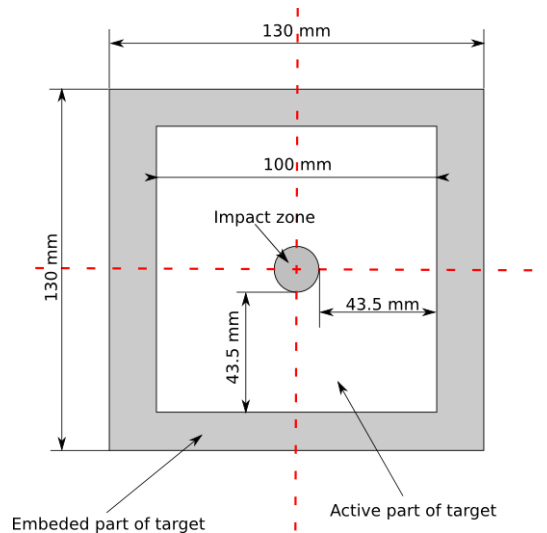
120

121 Perforation tests were conducted using a pneumatic gas gun to launch a projectile onto an AA 2024-
 122 T351 plate specimen, see Figure 1. The maximum velocity of the projectile, denoted as *impact velocity*
 123 V_0 , is reached at the end of the tube C. Both initial impact and residual velocities of the projectiles
 124 were measured during the impact tests using laser sensors attached to photodiodes and timers at D
 125 and F. The maximum error on the velocity measurements between the two sensors was estimated
 126 around $\Delta \bar{V} \approx 1 \text{ m/s}$. Further details of the experimental setup are provided in previous works [10;12].
 127 In addition, the set-up E may be instrumented to measure the force impact or force perforation on
 128 time as reported in [40] using four piezoelectric sensors with a maximum force of 80 kN.
 129



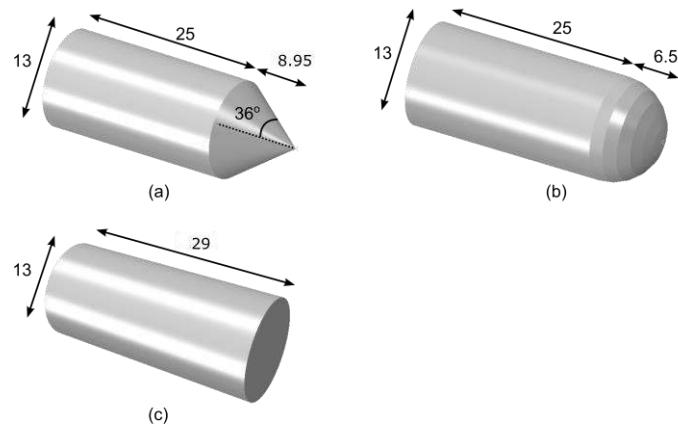
130
131
132 **Fig. 1:** Scheme of experimental set up used for perforation test.

134 The AA 2024-T351 specimens were clamped along four edges using a rigid support in order to reduce
 135 sliding effects during the test. This arrangement (screwing + clamping) has been discussed in previous
 136 works by the authors [10-11]. The active target area of the specimens was reduced to
 137 $100 \text{ mm} \times 100 \text{ mm}$ with a plate thickness of 4 mm, see Figure 2.
 138



139
140 **Fig. 2:** Geometry and dimensions of target.

142 The tests were conducted using three types of projectiles released at different impact velocities up to
 143 $V_0 \approx 200 \text{ m/s}$: The projectiles were made of a maraging steel with a heat treatment to reach a yield
 144 stress close to $\bar{\sigma}_y = 2 \text{ GPa}$. The projectiles, independently of the nose shape configuration, present a
 145 maximum diameter $\phi_{projectiles} = 13 \text{ mm}$ and a constant mass of $M_p \approx 30 \text{ g}$. Their geometries and
 146 dimensions are shown in Figure 3-a-c.



147
 148 **Fig. 3:** Geometry and dimensions (mm) of the projectiles used in the perforation test: a) conical
 149 projectile; b) hemispherical projectile; and c) blunt projectile.

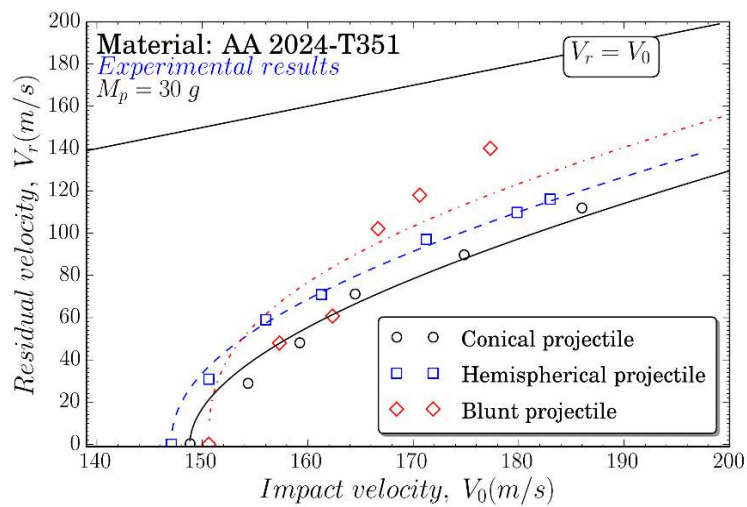
150
 151 The diameter of the projectiles was approximately equal to the diameter of the barrel to ensure a
 152 perpendicular impact on the aluminium plate.

153 **2.3 Experimental results**

154 **2.3.1 Residual velocity**

155 Figure 4 shows the residual velocity versus impact velocity ($V_r - V_0$) curves for the three different
 156 projectile-shapes considered. The ballistic limits (V_{bl}) were found to be 147.0 m/s, 148.8 m/s and
 157 150.6 m/s respectively for hemispherical nose, conical nose and blunt nose. This sequence of ballistic
 158 limits differs from previous results conducted on aluminium alloys AA 6082-T6 and AA 5754-H111
 159 (reported by Rodríguez-Millán and co-authors [12]).

160



161
 162 **Fig. 4:** Comparison of residual velocity V_r versus impact velocity V_0 between conical, hemispherical and
 163 blunt projectiles.

164

165 The results shown in Figure 5 have been fitted via the expression proposed by Recht and Ipson [31] as
 166 follows:

167

$$168 \quad V_r = (V_0^\kappa - V_{bl}^\kappa)^{1/\kappa} \quad (1)$$

169

170 where κ is a fitting parameter depending on the projectile shape that describes the trend of the
 171 relationship, determined as $\kappa = 1.92$ for the conical projectile; $\kappa = 2.13$ for the hemispherical
 172 projectile; and $\kappa = 2.61$ for the blunt projectile.

173

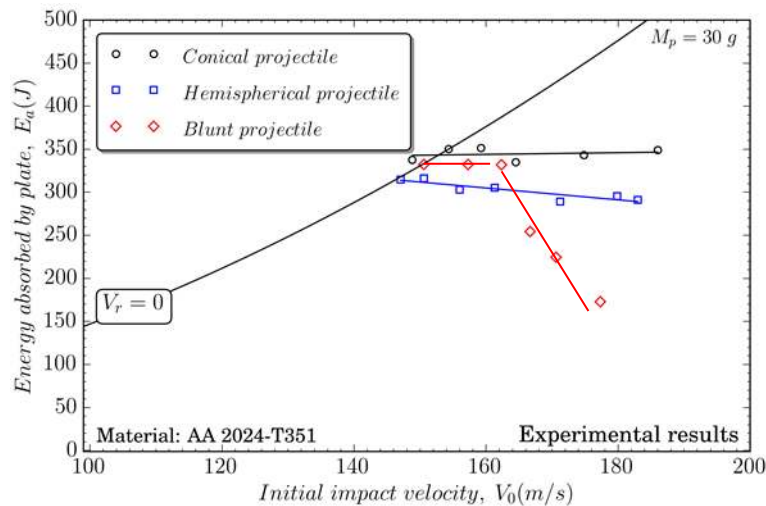
174 Figure 5 illustrates the amount of energy absorbed by the target versus impact velocity V_0 for the
 175 three projectile nose shapes considered. The energy absorbed by the plate, E_a , was calculated using
 176 the following expression:

$$177 \quad E_a = \frac{1}{2} \cdot M_p \cdot (V_0^2 - V_{bl}^2) \quad (2)$$

178

179 The energy absorbed by the target is almost independent on the initial velocity when the plate is
 180 impacted by conical projectiles (within the range of velocities tested), see Figure 5. The same behaviour
 181 was observed in a previous work for other two aluminium alloys: AA 5754-H111 and AA 6082-T6 [12].
 182 For the case of hemispherical projectiles, a slight variation in energy absorption with impact velocities
 183 can be noticed. In contrast, energy absorption sharply decreases as the impact velocity increases when
 184 the blunt projectile is used, see Figure 5.

185



186

187 **Fig. 5:** Energy absorbed by the target E_a versus impact velocity V_0 for conical, hemispherical and blunt
 188 projectiles.

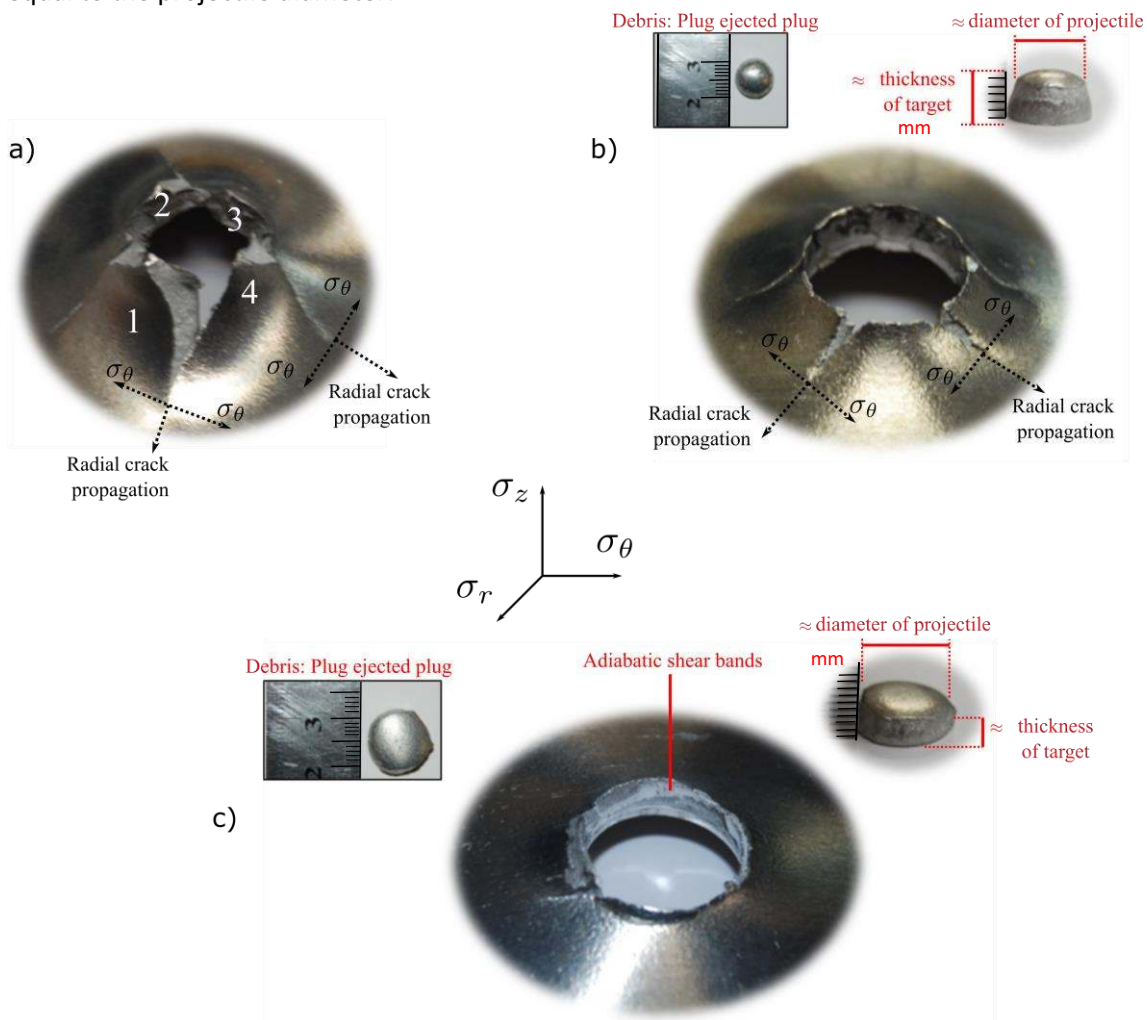
189

190 The different perforation mechanisms associated with the three nose-shaped projectiles considered
 191 explain the intersection shown in the $V_r - V_0$ curves (Figure 4) and in the $E_a - V_0$ curves (Figure 5).
 192 The larger ballistic limit of the blunt projectile is attributed to high yield stress of the AA 2024-T351,
 193 which enhances the critical impact velocity required for the shear bands formation. However, once the
 194 ballistic limit is exceeded, the energy consumed by this failure mechanism considerably decreases with
 195 impact velocity.

196 **2.3.2 Failure mode**

197 The variation in energy absorption capacity with different projectile nose shapes can be related to the
 198 corresponding difference in deformation and failure modes as shown in Figure 6. In this regard,
 199 Kpenyigba and co-authors [11] observed that the failure strain depends on the stress state induced by
 200 the projectile shape.

201
 202 When using conical projectiles in the range of impact velocities considered, the failure process occurs
 203 following petalling mechanisms, see Figure 6a. Four petals were observed in these tests, what has been
 204 frequently reported for metals [12; 33-33]. Hemispherical projectiles, in contrast, led to a plate failure
 205 based on ductile hole enlargement, where the material in front of the projectile is pushed forward, see
 206 Figure 6b. Localised rear bulging with radial cracks and short petals was also observed. The plug ejected
 207 shows a diameter similar to the projectile; however, the diameter of the perforated hole was found to
 208 be smaller than the projectile's due to elastic recovery (*spring back behaviour*). For the case of blunt
 209 projectile (Figure 6c), the failure mode of the plate was dominated by shear banding leading to the
 210 ejection of a circular plug at the final stage of the perforation. This circular plug presented a diameter
 211 equal to the projectile diameter.

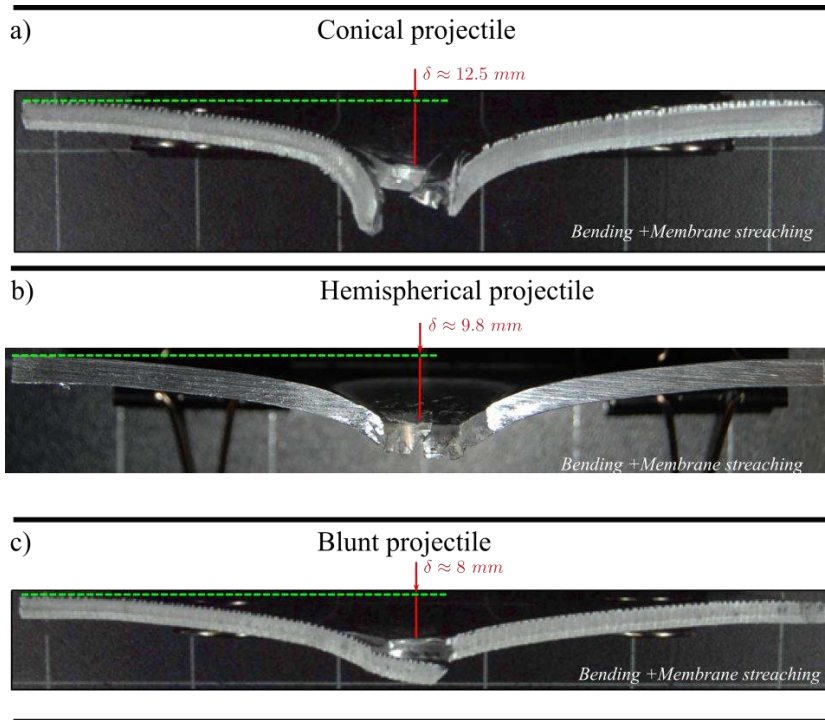


212
 213
 214 **Fig. 6:** Failure modes of the perforation process for the different projectiles: a) conical projectile, $V=175$
 215 m/s; b) hemispherical projectile, $V=171$ m/s; and c) blunt projectile, $v=168$ m/s.

216

217 The cross sections have been digitalized in order to analyze the global deformation. Figure 7 shows
218 cross sections of plates at velocities close to the ballistic limit for the three different projectile nose-
219 shapes. For the same impact velocity, the global deformation (bending and membrane stretching) was
220 higher when using the conical projectile configuration than for the other two configurations. However,
221 in the case of the blunt projectile configuration, the local failure mechanisms were more energy
222 consuming.

223
224
225



226
227

228 **Fig. 7:** Cross sections of penetrated plates by: a) conical projectile, $V=149 \text{ m/s}$; b) hemispherical
229 projectile, $V=147 \text{ m/s}$; and c) blunt projectile, $V=151 \text{ m/s}$.

230

231 In order to carry out a more extensive analysis of the problem, a numerical model is developed in next
232 section providing more information about the deformation and failure processes.

233

234 3. Numerical simulations

235 3.1 Thermoviscoplastic material behaviour

236

237 Although some authors have observed an anisotropic behaviour in AA 2024-T351 [34-35], its
238 mechanical behaviour is commonly defined by isotropic material models and von Mises yield function
239 [7,36]. Since the main objective of this work is to analyse the influence of triaxiality on the energy
240 absorption capability and how it affects the failure mechanisms that govern the perforation process,
241 the isotropic material definition adopted has been considered. In this regard, the thermoviscoplastic

242 material behaviour of AA 2024-T351 plates is defined by the Johnson-Cook (JC) model [37]. This
 243 hardening law defines the effective flow stress following the expression bellow, Eq. (3). The first term
 244 of Eq. (3) defines the strain hardening due to plastic deformation ($\bar{\epsilon}^p$) depending on the reference yield
 245 stress A and the material constants B and n . The second term accounts for strain rate sensitivity ($\dot{\epsilon}^p$)
 246 through the material parameter C and the reference strain rate $\dot{\epsilon}_0$. Regarding the third term, it
 247 captures the thermal softening on the material by the thermal sensitivity parameter m .

$$248 \quad \bar{\sigma}(\bar{\epsilon}^p, \dot{\epsilon}^p, T) = [A + B(\bar{\epsilon}^p)^n] \left[1 + C \ln \left(\frac{\dot{\epsilon}^p}{\dot{\epsilon}_0} \right) \right] [1 - \Theta^m] \quad (3)$$

249 Where Θ depends on the current temperature T , the melting temperature T_m and a reference
 250 temperature T_0 as:

$$252 \quad \Theta = \frac{T - T_0}{T_m - T_0} \quad (4)$$

253 The parameters of the constitutive equation were identified for AA 2024-T351 by Teng and Wierzbicki
 254 [36] and are provided in Table 1 with other physical properties. The Taylor-Quinney coefficient which
 255 defines the percentage of plastic work converted into heat, was taken equal to $\beta = 0.9$ [38]. The initial
 256 temperature T_0 was set to 293 K and the melting temperature T_m for this alloy is 775 K. **The density of
 257 the material is denoted by ρ and C_p is the specific heat at constant pressure.**

258 In addition, the numerical model implemented in this work takes into account the temperature
 259 evolution assuming adiabatic heating. This is computed along the deformation process through the
 260 expression [39]:

$$261 \quad \Delta T(\bar{\epsilon}^p, \dot{\epsilon}^p, T) = \frac{\beta}{\rho C_p} \int_{\bar{\epsilon}^e}^{\bar{\epsilon}^p} \bar{\sigma}(\bar{\epsilon}^p, \dot{\epsilon}^p, T) d\bar{\epsilon}^p \quad (5)$$

262

| Elasticity | | Thermoviscoplastic behaviour | | | | | |
|--------------------------|------------|------------------------------|----------|----------|-----------------------------|--------|--------|
| $E(GPa)$ | $\nu(-)$ | $A(MPa)$ | $B(MPa)$ | $n(-)$ | $\dot{\epsilon}_0 (s^{-1})$ | $C(-)$ | $m(-)$ |
| 70 | 0.3 | 352 | 440 | 0.42 | $3.3 \cdot 10^{-4}$ | 0.0083 | 1.7 |
| Other physical constants | | | | | | | |
| $\rho(kg/m^3)$ | $\beta(-)$ | $C_p(J/kg K)$ | $T_0(K)$ | $T_m(K)$ | | | |
| 2700 | 0.9 | 900 | 293 | 775 | | | |

263

264 **Table 1:** Properties of AA 2024-T351 and JC parameters [36].

265 3.2 SPH conversion criterion

266

267 The original mesh of the numerical model has been defined using Lagrangian elements. These
 268 elements are converted into SPH particles when a “flag variable” reaches a critical value. In this work,
 269 the equivalent plastic strain has been selected as the mechanical variable controlling the FEM-SPH
 270 conversion. The features of the model (initial, boundary conditions and contact interactions) are
 271 transferred appropriately when SPH particles are generated. The main advantage of the conversion
 272 approach over the SPH formulation is the reduction in the computational cost.

273 Therefore, a critical value of the equivalent plastic strain implies the conversion of the Lagrangian
 274 element into a sphere $\bar{\epsilon}^p \geq \bar{\epsilon}_{crit}^p$. Once the conversion of the elements is reached, due to the nature

275 of the impact problem, the SPH particles overpass the boundaries of their action domain leading to
 276 failure. The boundaries of this action domain are defined by a characteristic length that, if is small
 277 enough, allows the assumption of considering the conversion criterion as the failure one. The critical
 278 equivalent plastic strain is then directly related to failure and was found to vary with the nose shape
 279 of the projectiles. This suggests a dependence of $\bar{\epsilon}_{crit}^p$ on stress state. Then, the general form of this
 280 type of conversion strain can be expressed as Eq. (6):

$$281 \quad \bar{\epsilon}_{crit}^p = f(\eta) \quad (6)$$

282 Where η is the stress triaxiality defined by the ratio of the mean stress σ_m to the equivalent stress $\bar{\sigma}$.
 283 This conversion criterion model based on the level of failure strain is often used in dynamic problems
 284 [14-16]. According to several works [11, 36], the average value of the stress triaxiality can be slightly
 285 approximated just before the failure of the target for each projectile studied. Then, the triaxiality
 286 values have been determined from the components of the stress tensor in the elements of the failure
 287 zone prior to perforation.

288
 289 The critical values listed in Table 2 were identified for AA 2024-T351 based on an optimization process
 290 for the whole range of impact velocities considered depending on the projectile shape. The numerical
 291 optimization process minimized the error on the residual velocity with experiments. Figure 8 shows a
 292 comparison between the critical strain values obtained in this work and the failure strain values in a
 293 recent work of the authors [29], presenting good agreement between both results. These results
 294 provide validity of failure strain values employed in the present work. In addition, the numerical model
 295 provides faithfully predictions of postmortem deflections of the plates with respect to experiments. It
 296 can be concluded then, that the material failure during the perforation process is governed by
 297 irreversible deformation mechanisms that depend on the triaxiality value associated to each projectile
 298 shape.

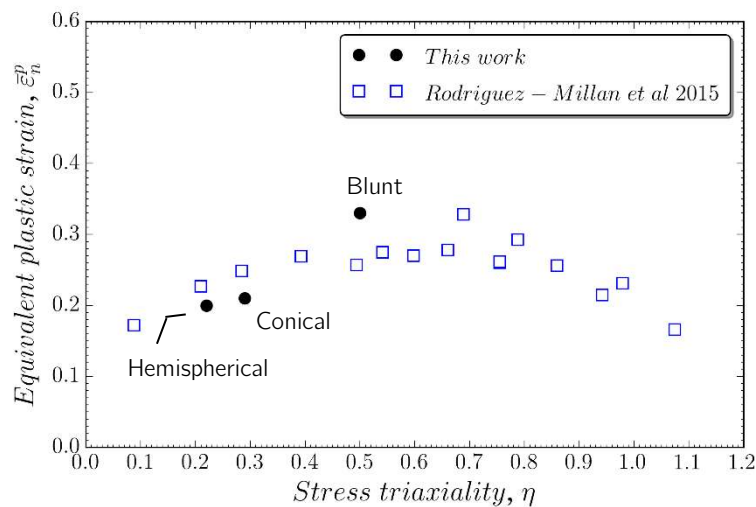
299

| Projectile shape | Conical | Hemispherical | Blunt |
|---------------------------|---------|---------------|-------|
| $\bar{\epsilon}_{crit}^p$ | 0.21 | 0.2 | 0.33 |

300

301 **Table 2:** Failure strain values used to simulate perforation depending on the projectile shape.

302



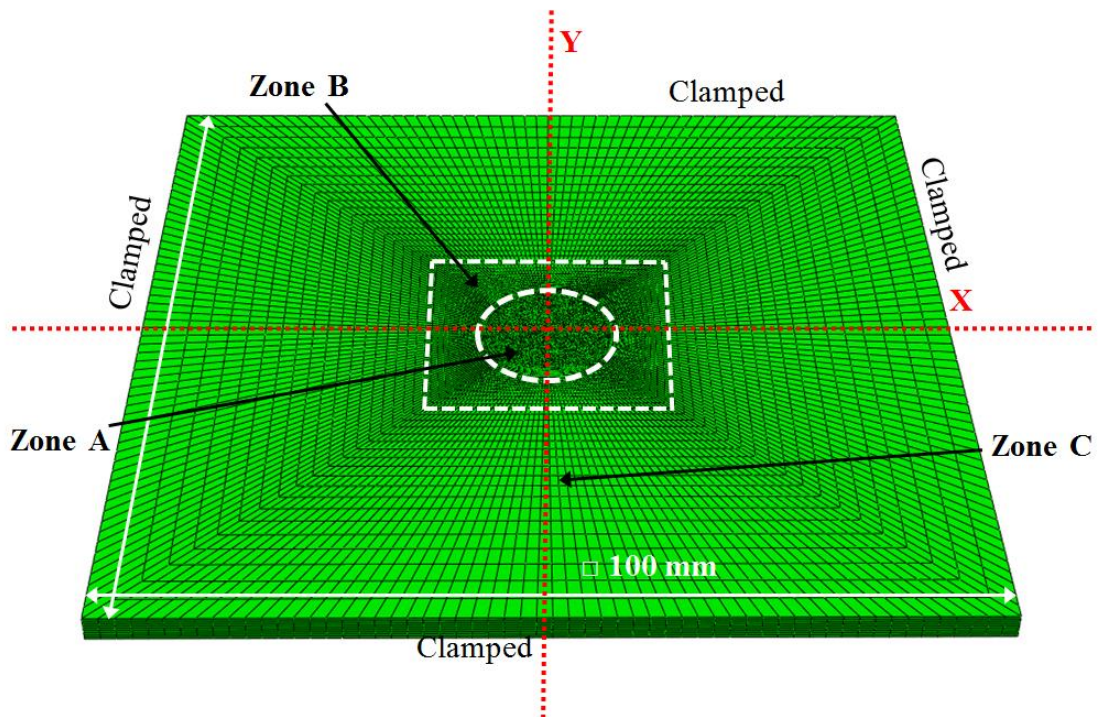
303

304 **Fig. 8:** Comparison of failure strain values between this work and data provided by Rodriguez-Millan
305 and co-authors [29].

306 **3.3 Mesh definition and boundary conditions used in numerical simulations**

307 The numerical simulations of the impact problem were carried out using the commercial software
308 ABAQUS 6.12/Explicit. The geometry of the targets and projectiles is the same as used in experiments.
309 The mesh of the target plate included a total number of 264100 nodes and 242500 elements, see
310 Figure 9. A total number of 12 elements were defined along the 4 mm thickness as recommended by
311 Rodríguez-Martínez and co-authors [9]. The mesh was divided into three different zones as follows
312 (see Figure 9):

- 313
- 314 • Zone A covers the contact region between the projectile and the target. The diameter of this
315 region is similar to the diameter of the projectile. A mesh with 34900 eight-node brick hexahedral
316 elements with one integration point, C3D8R in ABAQUS notation [23], was defined. These
317 elements may be converted into SPH (PC3D elements).
- 318 • Zone B covers the transition region between the fine mesh zone (centre of target) and coarse
319 mesh zone (boundary of target). The zone is defined by 44500 eight-node brick hexahedral
320 elements with one integration point, C3D8R in ABAQUS notation [23]. These elements may also
321 be converted into SPH (PC3D elements).
- 322 • Zone C covers the region that is located sufficiently far from the zone directly affected by the
323 impact. This zone was meshed using 163150 hexahedral elements, C3D8R.
- 324



325 **Fig. 9:** Target mesh used in the numerical simulations.
326

327

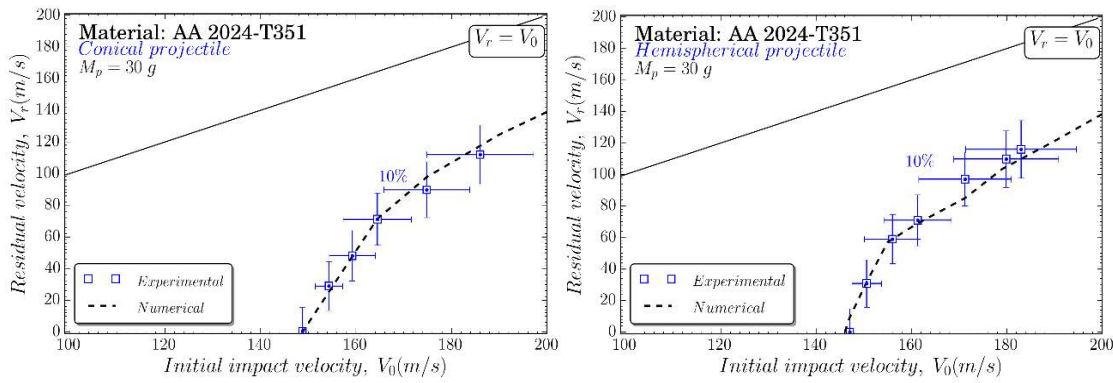
328 The projectiles were modelled with a nominal mass and a maximum diameter of 30 g and 13mm
 329 respectively. The projectile was defined as an analytical rigid body since experimental tests revealed
 330 no plastic deformation on the projectile-surface after impact. This definition allows for reducing the
 331 computational cost required in the simulations. A friction coefficient equal to 0.1 was used to define
 332 the contact between the projectiles and the plate, as done by several other authors [2,6,9,21,32].

333 **4. Numerical results and comparison with experimental data**

334 **4.1 Residual velocity**

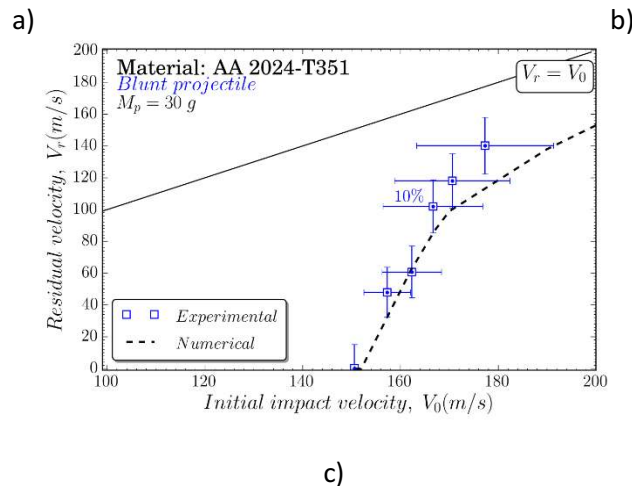
335

336 A comparison between experimental and numerical results in terms of residual versus impact
 337 velocities for different projectile nose shapes was carried out, see Figure 10. The use of a mesh density
 338 of 12 elements along the plate thickness was enough to simulate the perforation experiments
 339 accurately. The model provides a good correlation between numerical and experimental residual
 340 velocities depending on the impact velocity for the projectile shape configurations considered.



342

343



345

346

Fig. 10: Comparison of residual velocity V_r versus impact velocity V_0 between experiments and numerical simulations for: a) conical projectile; b) hemispherical projectile; and c) blunt projectile.

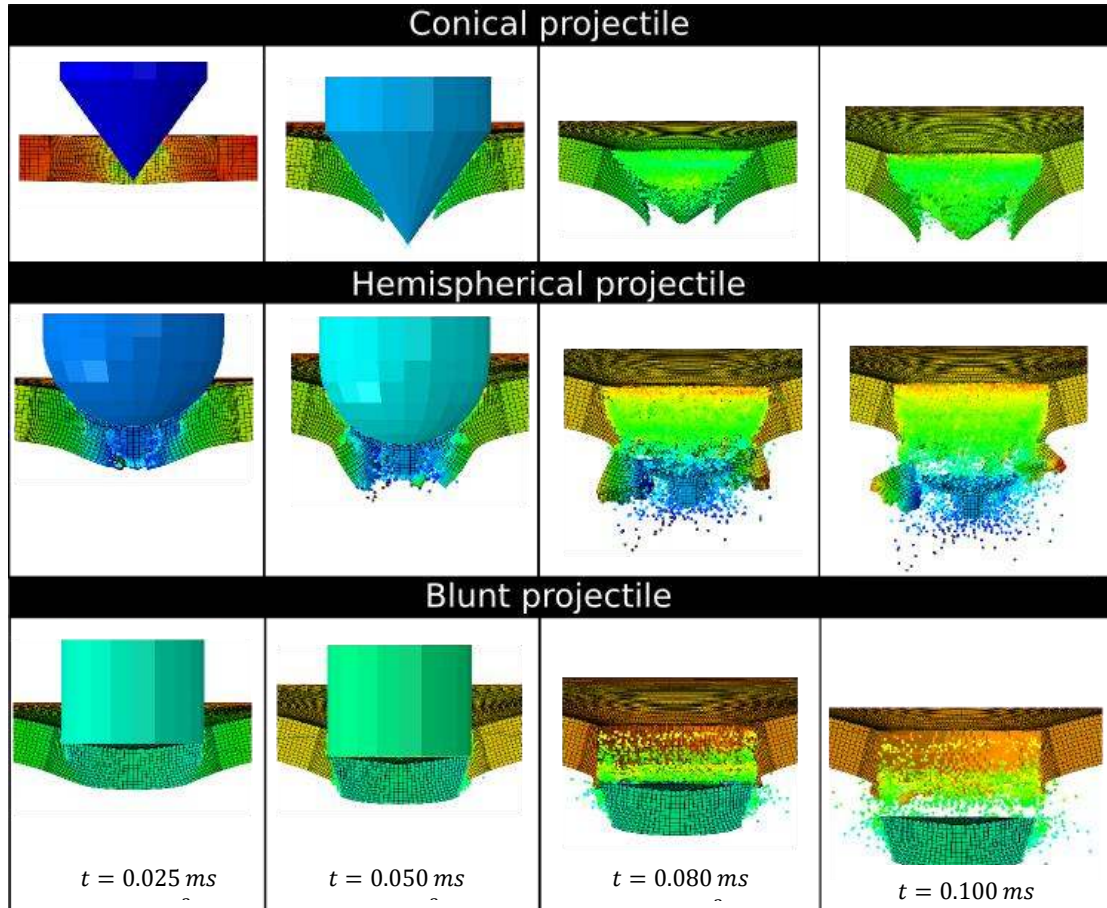
347

348 Once the model has been validated, it is used next to analyze the mechanisms behind the failure
 349 process.

350 **4.2 Failure Mechanism**

351

352 Figure 11 shows the perforation process for the three projectile configurations at three different
 353 stages. It can be observed that the largest density of SPH elements (converted from FEM) occurred
 354 when using the conical projectile nose.



355

356

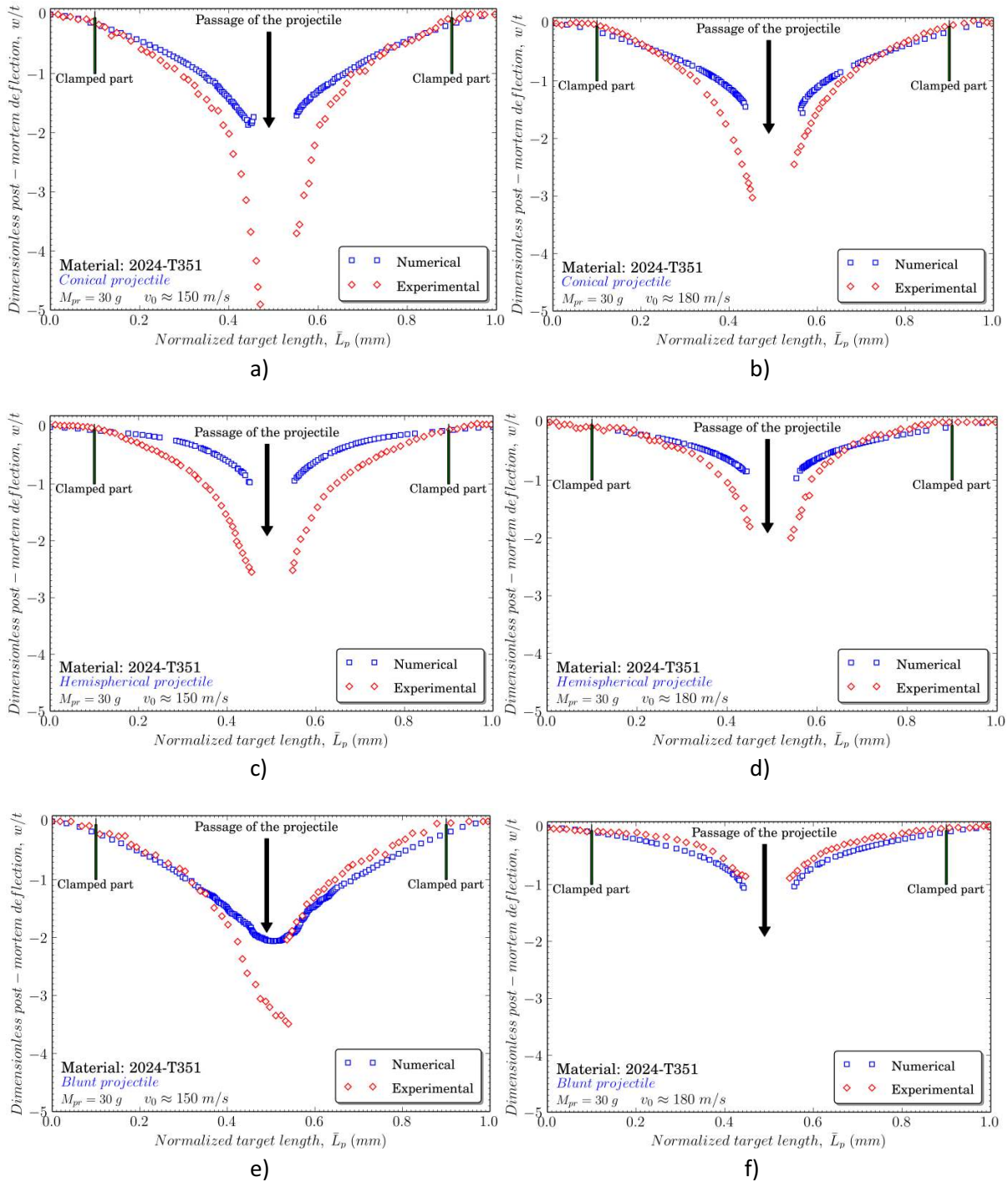
357 **Fig. 11:** Details of SPH element conversion and deformation behaviour of targets impacted at $v=170$
 358 m/s by: a) conical; b) hemispherical; and c) blunt projectiles. (For the sake of clarify, the projectiles are
 359 not displayed at $t=0.080$ and $t=0.100$ ms)

360

361 Different failure modes have been observed during the perforation tests. Figure 12 presents a
 362 comparison between experiments and numerical simulations in terms of permanent plate bending for
 363 two impact velocities: 150 m/s and 180 m/s. The y-axis corresponds to the normalized displacement
 364 of the impacted plates w/t (where w is the out-of-plane displacement and t is the target thickness);
 365 and the x-axis represents the normalized target length. The numerical model provides better
 366 predictions for impact velocities above the ballistic limit. The following general observations were
 367 drawn from this analysis.

368

- 369 • For all projectile configurations, the deflection is maximum at velocities close to the ballistic
 370 limit. This behaviour is in agreement with the observed in other aluminium alloys [12].
- 371 • In the case of the blunt projectile configuration, the model predictions of the plate deflection
 372 are better than for the other two configurations. This can be explained by the predominance
 373 of the global mechanism -bending- on the deformation process.



374
375

376
377

378
379

380 **Fig. 12:** Dimensionless post-mortem deflection of the plates as a function of the normalized target
 381 length for: (a) conical nose at $V_0 \sim 150$ m/s; (b) conical nose at $V_0 \sim 180$ m/s ; (c) hemispherical nose
 382 at $V_0 \sim 150$ m/s; (d) hemispherical nose at $V_0 \sim 180$ m/s; (e) blunt nose at $V_0 \sim 150$ m/s; and (f) blunt
 383 nose at $V_0 \sim 180$ m/s.

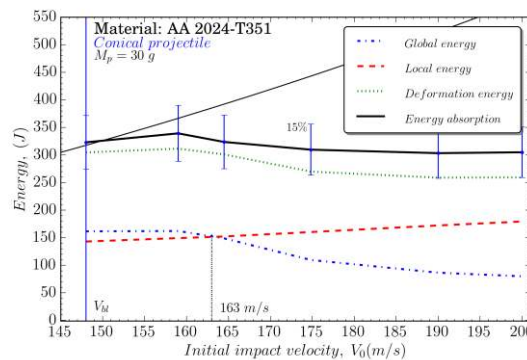
384 **4.3 Energy absorption capacity**

385 The total energy absorbed can be understood as the contribution of global and local deformations
 386 contributions. The present numerical modelling is necessary to develop a careful analysis of the energy
 387 absorbed by the plate within the impact velocity range considered. Thus, the target was modelled as

388 a local part (zone A in Figure 9) and a global part (zone B and C in Figure 9) with identical material
 389 properties. This allows for studying global versus local energy absorptions during penetration. In this
 390 work, the local energy absorption is associated with local failure mechanisms (shear, petalling and
 391 plugging); and the global energy absorption is associated with deformation mechanism (general
 392 bending).

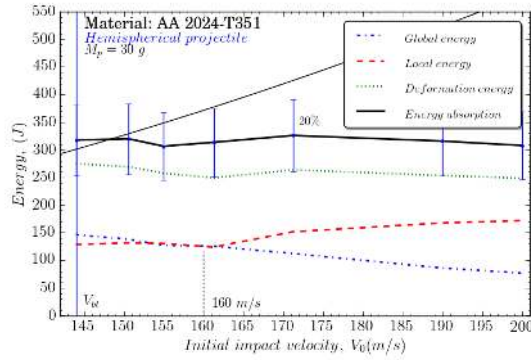
393
 394 The sensitivity of global (E_G), local (E_L), deformation (E_D) and absorption (E_A) energies to impact velocity
 395 is assessed for all projectiles, see Figure 13. The energy absorbed is defined as the difference between
 396 the initial and final kinetic energy, Eq. (2). The global energy (E_G) is the sum of internal energy of the
 397 elements of zones B and C (Figure 9), while the local energy (E_L) is the same sum but for the elements
 398 of the local region (zone A in Figure 9). The deformation energy $E_D = E_G + E_L$ is defined by the sum
 399 of local and global energies.

400
 401 For all nose shapes, it is remarkable that the local energy slightly increases while the global energy
 402 decreases with impact velocity. These results suggest that impact velocity is the variable that governs
 403 the main deformation mechanisms. As this variable increases, a progressive change can be observed
 404 from a global mechanical resistance to deformation associated with the overall response of the
 405 structure as a whole, to a local mechanical resistance associated with local deformation and failure
 406 mechanisms such as shearing, plugging or petalling. In addition, the global to local energy transition
 407 has been found to depend on the projectile nose shape and, therefore, on the triaxiality and failure
 408 mechanisms associated. For the case of blunt projectile, the thickness of plug is similar to the plate
 409 one. According to previous work [21], the adiabatic shear bands (ASB) velocity is faster than the initial
 410 impact velocity, inducing a failure by ASB propagation and obtaining local energy higher than global
 411 energy as demonstrated in Figure 13. In this regard, plugging mechanism associated with type of
 412 projectile shows the sharpest energy transition. Moreover, the evolution of these energies revealed
 413 15% to 20% differences between absorption energy and deformation energy for the three projectile
 414 configurations. Although some cracks propagate reaching zone B, the energy consumed in this region
 415 due to such effects can be neglected with respect to the energy associated to local energy in zone A.
 416 This issue has been analysed by varying the relative dimensions of both zones in order to keep the local
 417 cracks into zone A. The dimensions used in this work are consistent for the different configurations
 418 used in terms of energy evaluation.

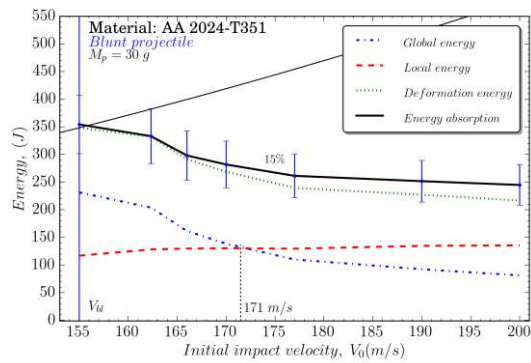


419
 420

a)



b)



c)

421
422

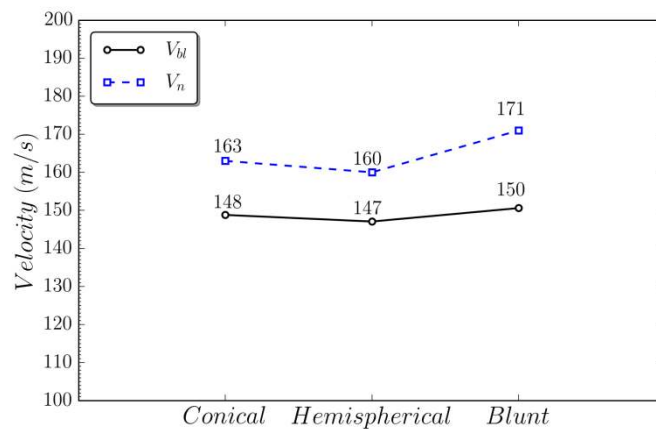
423

424

425 **Fig. 13:** Numerical prediction of the evolution of global, local, total and absorption energies versus
426 impact velocity for: a) conical; b) hemispherical; and c) blunt projectiles.

427

428 It can be also observed from Figure 13, that there is a velocity at which the global energy is equal to
429 the local energy; defined here as *neutral velocity*. For the sake of clarity, a bar chart comparison
430 between ballistic limit and neutral velocity for the three projectiles is presented in Figure 14. The
431 ballistic limit and neutral velocity seems to be dependent on projectile shape-nose. In this regards,
432 blunt projectile exhibits higher ballistic limit and neutral velocity than conical and hemispherical
433 projectiles.



434

435 **Fig. 14:** Differences between ballistic limit and neutral velocity for conical, hemispherical and blunt
436 projectile.

437

438 The observations mentioned above, reinforce the idea that the impact energy is absorbed by a
439 combination of local and global deformation mechanisms. It is also important to emphasize the need
440 of developing reliable numerical models in order to obtain accurate predictions of the mechanical
441 behaviour of materials under impact loading.

442 **5. Conclusions**

443

444 In this paper an experimental and numerical analysis of the influence of projectile geometry on the
445 ballistic performance of 2024-T351 aluminium alloy is presented. Projectiles with conical,
446 hemispherical and blunt nose shapes were considered. Residual velocities, failure mechanisms and
447 energy absorption during and after impact were investigated at velocities up to 200 m/s. The
448 conversion FEM-SPH method was used in this study providing accurate predictions of the mechanical
449 behaviour of AA 2024-T351 under impact loading. The simulations allowed for the understanding of
450 impact phenomena and deformation energy distribution along the aluminium plates. No significant
451 difference in the ballistic resistance was observed between three nose shape projectiles considered.
452 However, a relevant variation in residual velocity was noted as the impact velocity increases. The
453 amount of kinetic energy converted into global and local energy strongly depends on the nose-shape
454 of the projectile as revealed by numerical simulations. At low impact velocities, the global energy was
455 higher for blunt nose shape while at high impact velocities local energy was more significant for
456 hemispherical and conical nose shapes.

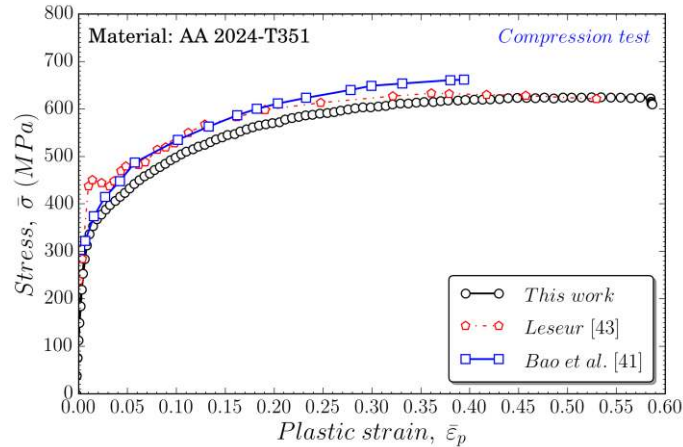
457 In conclusion, the stress state has been demonstrated to be a key variable in determining the failure
458 mechanisms and the FEM-SPH method has been found to be a valid way to analyze this influence in
459 impacts events.

460 **Acknowledgements**

461 The researchers are indebted to the Ministerio de Economía y Competitividad de España (Project
462 DPI2014-57989-P) for the financial support which permitted to conduct part of this work.

463 **Appendix A. Quasi-static tests on 2024-T351 aluminium alloy**

464 In order to verify the material used in this work and prior to identify the material parameters for its
465 mechanical modelling, quasi-static compression tests were performed. The results obtained from such
466 tests are in good agreement with the ones reported by other authors for this material [41-43], see Fig
467 A.1.



468

469 **Fig. A.1:** Quasi-static compression test for AA 2024-T351. Comparison of the stress-strain curve
 470 obtained for the material used in this work with published data.

471

472 In addition, the material parameters identified for the JC model used in this work have been compared
 473 with the ones provided by other authors, finding again a good agreement between them:

| A (MPa) | | | B (MPa) | | | n (-) | | |
|----------|-----------------|-----------|----------|-----------------|-----------|----------|-----------------|-----------|
| Our test | Bao et al. [41] | Error (%) | Our test | Bao et al. [41] | Error (%) | Our test | Bao et al. [41] | Error (%) |
| 329.3 | 352 | 6.44 | 431.7 | 440 | 1.88 | 0.36 | 0.42 | 14.2 |

474 **Fig. A.2:** Quasi-static compression test for AA 2024-T351. Comparison of the stress-strain curve
 475 obtained for the material used in this work with published data.

476 **References**

477

478 [1] National Highway Traffic Safety Administration-NHTSA (2014), Early Estimate of Motor Vehicle
 479 Traffic. Fatalities for the First Nine Months of 2013. Technical Report, U.S. Department of
 480 Transportation.

481 [2] Børvik T, Langseth M, Hopperstad OSS, Malo KA, Berstad T (2002) Perforation of 12 mm thick steel
 482 plates by 20 mm diameter projectiles with flat, hemispherical and conical noses Part II: numerical
 483 simulations. *Int. J. Impact Eng.* 27:37–64.

484 [3] Børvik T, Hopperstad OS, Langseth M, Malo KA (2003) Effect of target thickness in blunt projectile
 485 penetration of Weldox 460 E steel plates. *Int. J. Impact Eng.* 28(4): 413–464.

486 [4] Børvik T, Clausen AH, Hopperstad OS, Langseth M (2004) Perforation of AA5083-H116 aluminium
 487 plates with conical-nose steel projectiles—experimental study. *Int. J. Impact Eng.* 30(4):367–384.

488 [5] Gupta NK, Madhu V (1992) Normal and oblique impact of kinetic energy projectile on mild steel
 489 plates, *Int. J. Impact Eng.* 12(3): 333–343.

490 [6] Gupta NK, Iqbal MA, Sekhon GS (2006) Experimental and numerical studies on the behavior of thin
 491 aluminum plates subjected to impact by blunt- and hemispherical-nosed projectiles, *Int. J. Impact Eng.*
 492 32(12):1921–1944.

493 [7] Senthil K, Iqbal MA, Arindam B, Mittal R, Gupta NK (2017) Ballistic resistance of 2024 aluminium
494 plates against hemispherical, sphere and blunt nose projectiles, *Thin-Walled Structures*, Available
495 online 3 March 2017.

496 [8] Dey S, Børvik T, Hopperstad OS, Leinum JR, Langseth M (2004) The effect of target strength on the
497 perforation of steel plates using three different projectile nose shapes. *Int. J. Impact Eng.* 30(8-9):
498 1005–1038.

499 [9] Rodríguez-Martínez JA, Rusinek A, Pesci R, Zaera R (2013) Experimental and numerical analysis of
500 the martensitic transformation in AISI 304 steel sheets subjected to perforation by conical and
501 hemispherical projectiles. *Int. J. Solids Struct.* 50(2):339–351.

502 [10] Kpenyigba KM, Jankowiak T, Rusinek A, Pesci R (2013) Influence of projectile shape on dynamic
503 behavior of steel sheet subjected to impact and perforation, *Thin Wall. Struct.* 65:93-104.

504 [11] Kpenyigba KM, Jankowiak T, Rusinek A, Pesci R, Wang B (2015) Effect of projectile nose shape on
505 ballistic resistance of interstitial-free steel sheets, *Int. J. Impact Eng.* 79:83–94.

506 [12] Rodríguez-Millán M, Vaz-Romero A, Rusinek A, Rodríguez-Martínez JA, Arias A (2014)
507 Experimental Study on the Perforation Process of 5754-H111 and 6082-T6 Aluminium Plates Subjected
508 to Normal Impact by Conical, Hemispherical and Blunt Projectiles, *Exp. Mech.* 54(5):729–742.

509 [13] Manes A, Lumassi D, Giudici L, Giglio M (2013) An experimental–numerical investigation on
510 aluminium tubes subjected to ballistic impact with soft core 7.62 ball projectiles, *Thin Wall Struct*, 73:
511 68-80

512 [14] Mars J, Wali M, Jarraya A, Dammak F, Dhiab A (2015) Finite element implementation of an
513 orthotropic plasticity model for sheet metal in low velocity impact simulations, *Thin Wall Struct*, 89:93-
514 100.

515 [15] Dey S, Børvik T, Teng X, Wierzbicki T, Hopperstad OS (2007) On the ballistic resistance of double-
516 layered steel plates: An experimental and numerical investigation, *Int. J. Solids Struct* 44(20): 6701–
517 6723.

518 [16] Rusinek A, Rodríguez-Martínez JA, Zaera R, Klepaczko JR, Arias A, Sauvelet C (2009) Experimental
519 and numerical study on the perforation process of mild steel sheets subjected to perpendicular impact
520 by hemispherical projectiles, *Int. J. Impact Eng.* 36(4):565–587.

521 [17] Iqbal MA, Gupta NK (2011) Ballistic Limit of Single and Layered Aluminium Plates, *Strain. An Int.*
522 *Exp. Mech.* 47:205–219.

523 [18] Jankowiak T, Rusinek A, Wood P (2013) A numerical analysis of the dynamic behaviour of sheet
524 steel perforated by a conical projectile under ballistic conditions, *Finite Elem. Anal. Des.* 65: 39–49.

525 [19] Takaffoli M, Papini M (2009) Finite element analysis of single impacts of angular particles on
526 ductile targets, *Wear* 267:144–151.

527 [20] Campbell J, Vignjevic R (1997) Development of Lagrangian hydrocode modelling for debris impact
528 damage prediction, *Int. J. Impact Eng.* 20:143–152.

529 [21] Arias A, Rodríguez-Martínez JA, Rusinek A (2008) Numerical simulations of impact behaviour of
530 thin steel plates subjected to cylindrical, conical and hemispherical non-deformable projectiles, *Eng.*
531 *Fract. Mech.* 75:1635–1656.

532 [22] Rusinek A, Rodríguez-Martínez JA, Arias A, Klepaczko JRR, López-Puente J (2008) Influence of
533 conical projectile diameter on perpendicular impact of thin steel plate. *Eng. Fract. Mech.* 75 2946–
534 2967.

535 [23] Dassault Systèmes (2012) Abaqus v6.12 Documentation- ABAQUS analysis user's manual. ABAQUS
536 Inc; 6.12.

537 [24] Takaffoli M, Papini M (2012) Material deformation and removal due to single particle impacts on
538 ductile materials using smoothed particle hydrodynamics, *Wear* 274-275: 50–59.

539 [25] Johnson GR, Stryk RA, Beissel SR (1996) SPH for high velocity impact computations. *Comp.*
540 *Method. Appl. M.* 139:347–73.

541 [26] Zhang Z, Qiang H, Gao W (2011) Coupling of smoothed particle hydrodynamics and finite element
542 method for impact dynamics simulation, *Eng. Struct.* 33 255–264.

543 [27] Johnson GR (1994) Linking of Lagrangian particle methods to standard finite element methods for
544 high velocity impact computations, *Nucl. Eng. Des.* 150:265–74.

545 [28] Johnson GR, Beissel SR, Gerlach C (2013) A Combined Particle-element Method for High-velocity
546 Impact Computations. *Procedia Eng.* 58:269–278.

547 [29] Rodríguez-Millán M, Vaz-Romero Á, Arias, Á (2015) Failure behavior of 2024-T3 aluminum under
548 tension-torsion conditions. *J. Mech Sci. Technol.* 29(11): 4657-4663.

549 [30] Rodríguez-Martínez JA, Rusinek A, Chevrier P, Bernier R, Arias A (2010) Temperature
550 measurements on ES steel sheets subjected to perforation by hemispherical projectiles, *Int. J. Impact*
551 *Eng.* 37: 828–841.

552 [31] Recht RF, Ipson TW (1963) Ballistic Perforation Dynamics. *Journal of Applied Mechanics.*

553 [32] Rodríguez-Martínez JA, Rusinek A, Arias (2010) A Thermo-viscoplastic behaviour of 2024
554 T3 aluminium sheets subjected to low velocity perforation at different temperatures. *Thin Wall.*
555 *Struct.* 47:1268–1284.

556 [33] Atkins AG, Khan MA, Liu JH (2013) Experimental and numerical analysis of the martensitic
557 transformation in AISI 304 steel sheets subjected to perforation by conical and hemispherical
558 projectiles. *Int. J. Solid. Struct.* 50 339–351.

559 [34] Xue L (2007) Damage accumulation and fracture initiation in uncracked ductile solids
560 subject to triaxial loading, *Int J Solids Struct* 44 (16): 5163-5181.

561 [35] Steglich D, Brocks W, Heerens J, Pardoen T (2008) Anisotropic ductile fracture
562 of Al 2024 alloys, *Eng Fracture Mech* 75 (12):3692-3706.

563 [36] Teng X, Wierzbicki T (2005) Numerical study on crack propagation in high velocity perforation,
564 *Comput. Struct.* 83:989-1004.

565 [37] Johnson GR, Cook WH (1983) A constitutive model and data for metals subjected to large strains
566 high strain rates and high temperatures. In: *Proceedings of the seventh international symposium on*
567 *ballistics.*

568 [38] Garcia-Gonzalez D, Rodríguez-Millan M, Vaz-Romero A, Arias A (2015) High impact velocity on
569 multi-layered composite of polyether ether ketone and aluminium. *Compos. Interface*
570 <http://dx.doi.org/10.1080/09276440.2015.1051421>

571 [39] Garcia-Gonzalez D, Rusinek A, Jankowiak T, Arias A (2015) Mechanical impact behavior of
572 polyether-ether-ketone (PEEK). *Compos. Struct.* 124: 88-99.

573 [40] W.Z. Zhong, I.A. Mbarek, A. Rusinek, R. Bernier, T. Jankowiak, G. Sutter (2016) Development of an
574 experimental set-up for dynamic force measurements during impact and perforation, coupling to
575 numerical simulations, *Int. J. Impact Eng.*, 91:102–115.

576 [41] Y. Bao, T. Wierzbicki (2003) Prediction of Ductile Crack Formation in Uncracked Bodies.
577 Massachusetts Institute of Technology.

578 [42] X. Teng, T. Wierzbicki (2006) Evaluation of six fracture models in high velocity perforation. *Eng*
579 *Fract Mech*;73:1653–78.

580 [43] D.R.Lesuer (2000) Experimental investigations of material models for Ti-6Al-4V titanium and
581 2024-T3 aluminum. Lawrence Livermore National Laboratory. Report No.DOT/FAA/AR-00/25.,
582 <http://actlibrary.tc.faa.gov>.